Localization of gravitational wave sources with networks of advanced detectors

S. Klimenko,[1] G. Vedovato,[2] M. Drago,[3] G. Mazzolo,[4] G. Mitselmakher,[1]
C. Pankow,[1] G. Prodi,[3] V. Re,[5] F. Salemi,[4] and I. Yakushin[6]

[1]*University of Florida, P.O. Box 118440, Gainesville, Florida, 32611, USA*
[2]*INFN, Sezione di Padova, via Marzolo 8, 35131 Padova, Italy*
[3]*University of Trento, Physics Department and INFN, Gruppo Collegato di Trento, via Sommarive 14, 38123 Povo, Trento, Italy*
[4]*Max Planck Institut für Gravitationsphysik, Callinstrasse 38, 30167 Hannover and Leibniz Universität Hannover, Hannover, Germany*
[5]*INFN, Sezione di Roma Tor Vergata, Via della Ricerca Scientifica 1, 00133 Roma, Italy*
[6]*LIGO Livingston Observatory, Louisiana, USA*

(Received 19 January 2011; published 17 May 2011)

Coincident observations with gravitational wave (GW) detectors and other astronomical instruments are among the main objectives of the experiments with the network of LIGO, Virgo, and GEO detectors. They will become a necessary part of the future GW astronomy as the next generation of advanced detectors comes online. The success of such joint observations directly depends on the source localization capabilities of the GW detectors. In this paper we present studies of the sky localization of transient GW sources with the future advanced detector networks and describe their fundamental properties. By reconstructing sky coordinates of *ad hoc* signals injected into simulated detector noise, we study the accuracy of the source localization and its dependence on the strength of injected signals, waveforms, and network configurations.

DOI: 10.1103/PhysRevD.83.102001 PACS numbers: 04.80.Nn, 04.30.Db, 07.05.Kf, 95.55.Ym

I. INTRODUCTION

There has been a significant sensitivity improvement of gravitational wave detectors since the Laser Interferometer Gravitational Wave Observatory (LIGO) [1] and Virgo observatory [2] started their operation. In 2007 LIGO and Virgo completed a 2 yr run at a sensitivity that allows detection of a merger of two neutron stars (NS-NS) as far as ~30 Mpc away [3,4]. In the most recent run (May 2009–October 2010) the binary neutron star horizon distance has been increased to ~40 Mpc. However, even at this impressive sensitivity, the anticipated detection rate with the initial LIGO and Virgo detectors is quite low. A detection may be possible in the case of a rare astrophysical transient event such as a supernova explosion in our Galaxy or a nearby merger of binary neutron stars. The signal is likely to be weak, and it will be difficult to prove its astrophysical origin unless it is confirmed with a coincident observation of the electromagnetic or neutrino counterpart. For this reason the LIGO and Virgo collaborations are conducting a wide range of joint observations [5] with other astrophysical experiments including radio [6,7], optical, and x-ray telescopes [8–11], and neutrino detectors [12,13].

A more robust detection of gravitational waves from astrophysical sources is anticipated in the next five years as Advanced LIGO and Advanced Virgo come online. Numerous GW signals, expected to be observed by advanced detectors (likely ~40 NS-NS events per year [14]), will begin our exploration of the gravitational wave sky and start the era of gravitational wave astronomy. Along with the advanced GW detectors, a new generation of optical telescopes will come online [15–17], which will enable a wide and deep survey of the electromagnetic sky. Joint observations with the advanced gravitational wave detectors and electromagnetic instruments will not only increase the confidence of detection but also bring fundamentally new information about the GW sources. They will reveal the physics and dynamics of sources, provide identification of host galaxies and the associated redshifts, and in some cases determine the luminosity distance to the source.

One of the major challenges for such joint observations is to establish an unambiguous association between a gravitational wave signal and a possible electromagnetic (EM) counterpart. This greatly depends on the ability of the GW networks to reconstruct sky coordinates of a detected GW source. Given an accurate sky location, a corresponding EM transient may be identified in a list of events obtained with the all-sky telescope surveys, or the EM instruments can be guided to take images of a small area in the sky. In the second case, it is important that the sky localization is performed by GW detectors in real time with low latency. The efficiency of the GW-EM association and the choice of a partner telescope are affected by the sky localization error which should be well within the instrument's field of view (typically less than a few square degrees). Moreover, exploring a smaller area in the sky will decrease the probability of the false association.

The problem of the source localization with networks of GW detectors is one of the focuses of research on the gravitational wave data analysis. There are several analytical studies [18–21] of this problem that consider geometrical reconstruction of source coordinates based on the triangulation, which requires a measurement of the arrival

time of a GW signal at different detectors. However, the accurate timing of the GW signal is intimately related to the reconstruction of the signal waveforms. Because of the different detector sensitivities to the GW polarizations, the waveforms recorded by individual detectors may be different and they may not have a common timing reference (like a signal peak time) for a direct measurement of the differences in the arrival time. Therefore, the problem of the source localization is better addressed in the framework of the coherent network analysis [22–24], which reconstructs the waveforms and the sky coordinates simultaneously. By using both these methods (triangulation and coherent network analysis), several practical source localization algorithms [25–27] have been recently developed and used during the LIGO and Virgo data taking runs from 2009–2010.

There have been a number of studies addressing the benefits of individual detectors [28,29] and various detector networks [30,31]. In this paper we present a simulation study of the source localization and the reconstruction of GW waveforms with networks of advanced detectors. The study is performed with a coherent network method, called coherent WaveBurst [25] (cWB), based on the likelihood analysis. In cWB the data from all detectors in the network are processed simultaneously in order to reconstruct a common GW signal which is consistent with the recorded detector responses. The consistency is measured by the likelihood ratio, which is a function of the source parameters (waveforms and sky location). The most probable source parameters are obtained by maximizing the likelihood ratio over the signal waveforms and sky coordinates. The method performs reconstruction of unmodeled burst signals (arbitrary waveforms) and signals with a certain polarization state: elliptical, linear, and circular.

The paper is organized as follows. Possible networks of advanced detectors and their fundamental properties are discussed in Sec. II. In Sec. III we describe the reconstruction algorithm. The simulation framework for this study is presented in Sec. IV. The results are reported in Sec. V. In Secs. VI and VII we describe the main factors limiting the source reconstruction and discuss the results.

II. DETECTOR NETWORKS

From 2001–2010 the LIGO Scientific Collaboration (LSC) and the Virgo Collaboration operated a network of interferometric gravitational wave detectors which are the most sensitive instruments from the first generation of the GW interferometers (1G). They consist of power-recycled Michelson interferometers with kilometer-scale Fabry-Perot arms designed to detect gravitational waves with frequencies between tens of Hz and several kHz. The two LIGO observatories [1] are in Hanford, Washington (4 km and 2 km detectors) and in Livingston, Louisiana (4 km detector), and the 3 km Virgo detector [2] is located in Cascina, Italy. Other gravitational wave interferometers are

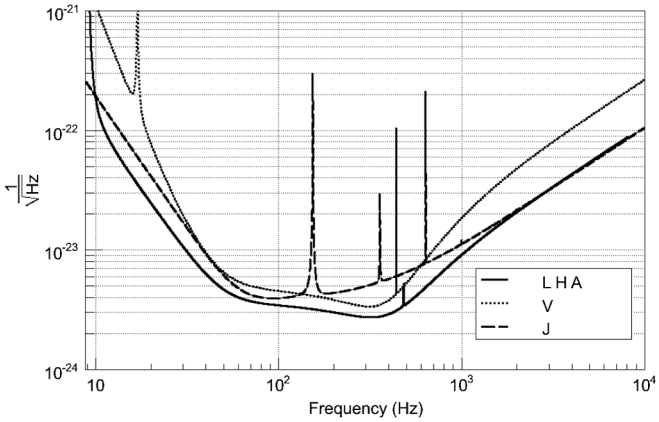

FIG. 1. Amplitude spectral density of the design noise for the second-generation detectors.

the 300 m detector TAMA [32] in Mitaka, Japan, and the 600 m detector GEO600 [33] in Hannover, Germany. Currently, all 1G interferometers are decommissioned, except Virgo and GEO600, which continue to take data.

The second-generation GW detectors (2G) are currently under construction. They include the advanced LIGO detectors [34], and the advanced Virgo detector (V) [35], which will have an order of magnitude better sensitivity than the 1G detectors. All advanced LIGO detectors have 4 km long arms, with one detector in Livingston (L) and two identical coaligned detectors in Hanford (H and $\tilde{\text{H}}$). Also, there are plans to build the Large Cryogenic Gravitational Telescope (LCGT) [36,37] in Japan (the J detector) and possibly move the LIGO $\tilde{\text{H}}$ detector to a site in Australia [30,38] (the A detector). Figure 1 shows the design sensitivity for the listed 2G detectors. These interferometers (hopefully all five) will compose the most advanced GW detector network planned for operation after 2015.

The network performance greatly depends on the number of detectors in the network, their location, and the orientation of the detector arms. Table I shows the geographical coordinates of the instruments and the orientation of the detector arms used in this study. For the Australian instrument the orientation of the detector arms is not yet decided; therefore, we consider two possible configurations: $\tilde{\text{A}}$ arms are due north and east, and A

TABLE I. Geographical locations and orientations of the 2G detectors. The orientation of the detector arms is defined by the rotation angle (counterclockwise) with respect to the local coordinate frame with axes due north and east.

Detector	Latitude	Longitude	Orientation
A	31°21′30″S	115°42′30″E	45.0°
H	46°27′18″N	119°24′27″W	126.0°
J	36°15′00″N	137°10′48″E	19.0°
L	30°33′46″N	90°46′27″W	197.7°
V	43°37′53″N	10°30′16″E	70.6°

arms are rotated counterclockwise by 45° with respect to Ã. Depending on what instruments are constructed, we consider several network configurations: HLV, HH̃LV, AHLV, HJLV, and AHJLV. Since the sky localization performance is expected to be about the same for the HLV and HH̃LV networks, only the HLV network was considered for the coordinate reconstruction studies.

A. Network sensitivity

The sensitivity of the network of K detectors is fully characterized by its noise-scaled antenna pattern vectors $\mathbf{f}_+$ and $\mathbf{f}_\times$:

$$\mathbf{f}_{+(\times)}[i] = \left(\frac{F_{1+(\times)}}{\sqrt{S_1[i]}}, \ldots, \frac{F_{k+(\times)}}{\sqrt{S_k[i]}}, \ldots, \frac{F_{K+(\times)}}{\sqrt{S_K[i]}}\right), \quad (2.1)$$

where $S_k[i]$ is the power spectral density (PSD) of the noise [39] and $(F_{k+}, F_{k\times})$ are the antenna patterns of individual detectors. $S_k[i]$ is a function of the time-frequency index i, which is replacing the separate time and frequency indices. Below in the text the index i is often omitted. Given the time-frequency series $x_k[i]$, obtained from a discrete detector output with an appropriate (in our case, wavelet) transformation,
$S_k[i]$ can be calculated for every data sample. Such time-frequency PSD "maps" are convenient for the characterization of the colored quasistationary noise of real detectors. The power spectral density $S_{\rm net}$ of the network noise is defined by the following equation:

$$S_{\rm net} = \left(\sum_{k=1}^{K} S_k^{-1}\right)^{-1}. \quad (2.2)$$

Note that the $S_{\rm net}$ decreases as more detectors are added to the network. A network of K equally sensitive detectors has, by a factor $\sqrt{K}$, a lower noise amplitude than the individual detectors. The utility of the network power spectral density is explained later in this section.

The antenna patterns depend upon the source coordinates (θ, ϕ) and the polarization angle Ψ, which defines the wave frame of the two-component GW signal $\mathbf{h}[i] = (h_+[i], h_\times[i])$. It is convenient to define vectors $\mathbf{f}_+$, $\mathbf{f}_\times$, and $\mathbf{h}$ in the dominant polarization wave frame [24], where $(\mathbf{f}_+ \cdot \mathbf{f}_\times) = \mathbf{0}$ and $|\mathbf{f}_+| \geq |\mathbf{f}_\times|$. The vectors $\mathbf{f}_+$ and $\mathbf{f}_\times$ define a vector of the noise-scaled detector responses to the wave $\mathbf{h}$,

$$\boldsymbol{\xi}_{\rm h}[i] = \mathbf{f}_+[i]h_+[i] + \mathbf{f}_\times[i]h_\times[i]. \quad (2.3)$$

The inner product $(\boldsymbol{\xi}_{\rm h}|\boldsymbol{\xi}_{\rm h})$ calculated over the sampled detector responses gives the estimator of the network signal-to-noise ratio (SNR):

$$\rho_{\rm net} = (\boldsymbol{\xi}_{\rm h}|\boldsymbol{\xi}_{\rm h})^{1/2}. \quad (2.4)$$

The inner product of two sets of vectors $\mathbf{a}$ and $\mathbf{b}$ with an arbitrary number of components is defined via their scalar products

$$(\mathbf{a}|\mathbf{b}) = \sum_i (\mathbf{a}[i] \cdot \mathbf{b}^*[i]), \quad (2.5)$$

where $\mathbf{b}^*$ is the complex conjugate of $\mathbf{b}$ and the sum is taken over the data samples i containing the signal [40].

The norms of the antenna pattern vectors $|\mathbf{f}_+|$ and $|\mathbf{f}_\times|$ characterize the network sensitivity to the GW polarizations. To illustrate this and other network properties, we assume below that in the signal frequency band the vectors $\mathbf{f}_+$ and $\mathbf{f}_\times$ do not vary much. In this case

$$\rho_{\rm net} \approx \sqrt{|\mathbf{f}_+|^2(h_+|h_+) + |\mathbf{f}_\times|^2(h_\times|h_\times)}, \quad (2.6)$$

where the inner product $(\mathbf{h}|\mathbf{h}) = (h_+|h_+) + (h_\times|h_\times)$ determines the root-sum-square amplitude of the GW polarizations:

$$h_{\rm rss} = (\mathbf{h}|\mathbf{h})^{1/2}. \quad (2.7)$$

As it follows from Eq. (2.6), the network alignment factor [25]

$$\alpha = |\mathbf{f}_\times|/|\mathbf{f}_+| \quad (2.8)$$

characterizes the relative network sensitivity to the two GW polarizations. It determines the ratio of the SNRs from each GW component, assuming that, on average, their sum-square energies are the same: $(h_+|h_+) = (h_\times|h_\times)$. Closely aligned networks (like HH̃L) have poor sensitivity to the second polarization ($\alpha \ll 1$), making reconstruction of the full GW signal difficult.

The overall network sensitivity is characterized by the effective power spectral density of the network noise,

$$N_{\rm net} = (|\mathbf{f}_+|^2 + |\mathbf{f}_\times|^2)^{-1}, \quad (2.9)$$

which depends on the sky coordinates. It is convenient to factorize the sky-dependent part of the effective power spectral density as

$$N_{\rm net} = \mathcal{F}^{-2} S_{\rm net}, \quad (2.10)$$

where $\mathcal{F}$ is the network antenna factor distributed between 0 (low sensitivity) and 1 (high sensitivity). $S_{\rm net}$ characterizes the sky-independent sensitivity of the network. These network parameters determine the average network SNR for a population of GW signals with the average amplitude $h_{\rm rss}/\sqrt{2}$ per polarization:

$$\bar{\rho}_{\rm net} \approx \frac{h_{\rm rss}}{\sqrt{2N_{\rm net}}} = \frac{\mathcal{F} h_{\rm rss}}{\sqrt{2S_{\rm net}}}. \quad (2.11)$$

The network PSD $S_{\rm net}$ defines the baseline noise, and the antenna factor $\mathcal{F}$ defines the fraction of the $h_{\rm rss}$ amplitude utilized by the network.

Figure 2 shows the antenna and the alignment factors for different networks as a function of the latitude and longitude of the source (sky maps). Since these network parameters are noise dependent, the sky maps are

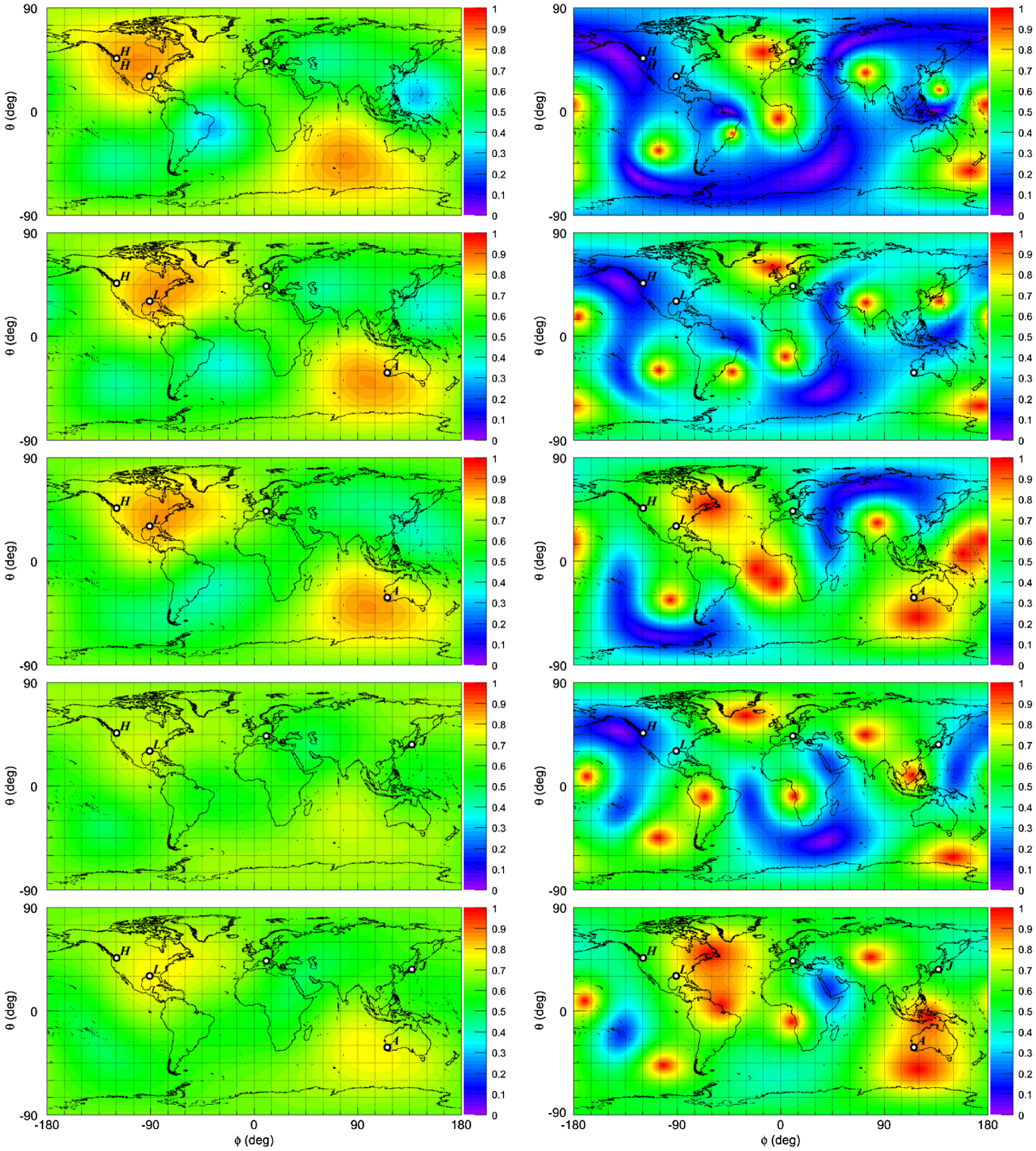

FIG. 2 (color online). The distributions of the network antenna factor $\mathcal{F}$ (left plots) and the network alignment factor α (right plots) at the frequency of 100 Hz as a function of latitude (θ) and longitude (ϕ) for the networks HH̃LV, ÃHLV, AHLV, HJLV, and AHJLV (from top to bottom).

calculated at the frequency 100 Hz, where the advanced detector sensitivities are about the same. The $\mathcal{F}$ distribution shows the network efficiency to capture the signal and its uniformity across the sky. The values of α close to unity indicate the same sensitivity to the two GW components. Respectively, the values of α close to zero indicate that the second GW component is not measurable for a weak GW signal. As Fig. 2 shows, several nonaligned detectors

TABLE II. Expected difference in detection rates with respect to the HLV network.

	HLV	HH̃LV	AHLV	HJLV	AHJLV
100 Hz	1	1.66	1.65	1.39	2.09
300 Hz	1	1.65	1.63	1.15	1.80

(preferably five) are required for the elimination of these blind spots in the sky.

One of the main characteristics of a detector network is its search volume. Given an isotropic distribution of transient sources with the root-square-sum amplitude h_o at the fiducial distance r_o, the search volume is defined as [41]

$$V_{\rm net} = 4\pi(h_o r_o)^3 \int_0^\infty dh h^{-4} \epsilon(h), \tag{2.12}$$

where ϵ is the detection efficiency. Assuming the same SNR thresholds $\rho_{\rm net}(h)$ [see Eq. (2.11)], the $V_{\rm net}$ can be calculated with respect to the volume V_0 of the reference network,

$$V_{\rm net} = V_0 \frac{\langle N_0^{3/2}\rangle}{\langle N_{\rm net}^{3/2}\rangle}, \tag{2.13}$$

where $\langle N_{\rm net}^{3/2}\rangle$ and $\langle N_0^{3/2}\rangle$ are the averages over the sky. The ratio $V_{\rm net}/V_0$ is quite independent on a search algorithm and a GW source model. Table II shows the volume (and detection rate) ratios calculated with respect to the HLV network ($V_0 = V_{\rm HLV}$). As more detectors are added to the network the detection rates increase. This increase can be beneficial; however, it is not critical for a first direct observation of gravitational waves. More importantly, the networks with more detectors are likely to be less affected by non-Gaussian and nonstationary noise than the networks with fewer detectors. They are expected to have lower false alarm rates and higher detection confidence for the same $\rho_{\rm net}$ threshold. Also, relocation of the LIGO H̃ detector to Australia does not affect the detection rates for the A and Ã configurations. But, as shown in Fig. 2, the AHLV detector configuration would be more preferable for the reconstruction of the GW polarizations than the HH̃LV or the ÃHLV network.

III. RECONSTRUCTION ALGORITHM

A. Coherent network analysis

One possible approach to the coherent network analysis is based on the Neyman-Pearson criterion which defines the likelihood ratio

$$\Lambda(\mathbf{x}, \Omega) = \frac{p(\mathbf{x}|\mathbf{h}(\Omega))}{p(\mathbf{x}|0)}, \tag{3.1}$$

where $\mathbf{x}$ is the network data, $p(\mathbf{x}|0)$ is the joint probability that the data are only instrumental noise, and $p(\mathbf{x}|\mathbf{h})$ is the joint probability that a GW signal $\mathbf{h}$ is present in the data. In general, the likelihood ratio is a functional which depends upon the source parameters Ω. One generalization of the Neyman-Pearson criterion is to maximize $\Lambda(\mathbf{x}, \Omega)$ over Ω. The obtained maximum likelihood ratio statistic reaches its maximum for the best match of the corresponding waveform to the data. If the source model allows the calculation of the GW waveforms as a function of a small number of source parameters (for example, for binary black holes), then a template bank can be generated. In this case the variation is performed over the template bank and the likelihood approach is equivalent to a matched filter. The cWB algorithm searches for unmodeled burst signals. In contrast to the binary black hole sources, where the number of parameters is relatively small, the parameters characterizing the unmodeled bursts are essentially the signal amplitudes themselves at each instance of time. It is not possible to generate a template bank for such a large parameter space. Instead, the best matching waveform is found by variation of Λ over unknown GW waveforms $\mathbf{h}$.

B. GW waveforms

For stationary Gaussian noise the coherent WaveBurst algorithm defines the likelihood $\mathcal{L}$ as twice the logarithm of the likelihood ratio Λ,

$$\mathcal{L}[\mathbf{h}] = 2(\mathbf{w}|\boldsymbol{\xi}_{\rm h}) - (\boldsymbol{\xi}_{\rm h}|\boldsymbol{\xi}_{\rm h}), \tag{3.2}$$

where the vector $\mathbf{w}$ represents whitened data from K detectors with uncorrelated noise,

$$\mathbf{w}[i] = \left(\frac{x_1[i,\tau_1]}{\sqrt{S_1[i]}}, \ldots, \frac{x_k[i,\tau_k]}{\sqrt{S_k[i]}}, \ldots, \frac{x_K[i,\tau_K]}{\sqrt{S_K[i]}}\right). \tag{3.3}$$

The sampled detector amplitudes (where i is a sample index) $x_k[i,\tau_k]$ take into account the time-of-flight delays τ_k, which in turn depend upon the source coordinates θ and ϕ. The solutions for the GW waveforms $\mathbf{h}$, defined in the dominant polarization frame, are found by the variation of the likelihood functional [Eq. (3.2)]:

$$H_+[i] = (\mathbf{w}[i]\cdot\mathbf{f}_+[i])/|\mathbf{f}_+[i]|^2, \tag{3.4}$$

$$H_\times[i] = (\mathbf{w}[i]\cdot\mathbf{f}_\times[i])/|\mathbf{f}_\times[i]|^2. \tag{3.5}$$

The maximum likelihood ratio statistic is calculated by substituting the solutions into $\mathcal{L}[\mathbf{h}]$. The result can be written as

$$L_{\rm max} = \sum_i \mathbf{w}[i]P[i]\mathbf{w}^T[i], \tag{3.6}$$

where the matrix P is the projection constructed from the components of the unit vectors $\mathbf{e}_+$ and $\mathbf{e}_\times$ along the directions of the $\mathbf{f}_+$ and $\mathbf{f}_\times$, respectively:

$$P_{nm}[i] = e_{+n}[i]e_{+m}[i] + e_{\times n}[i]e_{\times m}[i]. \tag{3.7}$$

The kernel of the projection P is the signal plane defined by these two vectors. The null space of the projection P defines the reconstructed detector noise which is referred to as the null stream.

The projection matrix is invariant with respect to the rotation in the signal plane, where any two orthogonal unit vectors can be used for the construction of the P_{nm}. Therefore, one can select the two orthogonal unit vectors $\mathbf{u}$ and $\mathbf{v}$ such that $\mathbf{w} \cdot \mathbf{v} = 0$ and then

$$P_{nm}[i] = u_n[i]u_m[i]. \tag{3.8}$$

The unit vector $\mathbf{u}$ defines the vector

$$\boldsymbol{\xi}[i] = (\mathbf{w}[i] \cdot \mathbf{u}[i])\mathbf{u}[i] \tag{3.9}$$

whose components are the standard likelihood estimators of the noise-scaled detector responses $\xi^k_{\mathrm{h}}[i]$.

C. Source coordinates

The maximum likelihood ratio statistic $L_{\max}$ is a function of the sky coordinates θ and ϕ. If no information regarding the source coordinates is available, then the variation over the sky should also be performed. It is expected that $L_{\max}$ takes a maximum close to a true source location; however, it is not necessarily the optimal statistic for the coordinate reconstruction. The coherent part of the likelihood quadratic form

$$E_c = \sum_i \sum_{n,m} w_n[i]w_m[i]P_{nm}[i], \qquad n \neq m \tag{3.10}$$

has a strong dependence on the time delays between the detectors, and therefore the coherent energy E_c is expected to be a better statistics for the source localization. On the other hand, the E_c is a biased estimator: for an arbitrary GW signal it may take a maximum value away from the true source location. To minimize the bias, the sky statistic is constructed in the following way:

$$L_{\mathrm{sky}} = \frac{L_{\max}E_c}{E(E - L_{\max} + |E_c|)}, \tag{3.11}$$

where $E = (\mathbf{w}|\mathbf{w})$ is the total normalized energy in the network data stream. This statistic penalizes the sky locations with low values of E_c and large values of the residual (null) energy $E - L_{\max}$. The L_{sky} reduces to the maximum likelihood statistic $L_{\max}/E$ when the ratio $(E - L_{\max})/E_c$ is close to unity, which is expected at the true source location. L_{sky} is used to rank different sky locations and calculate the probability distribution of the estimated source coordinates in the sky.

D. Model-dependent constraints

The likelihood method offers a convenient framework for the introduction of constraints arising from the source models. Unlike for template searches where accurate waveforms are required, in principle, any useful information about sources can be used to constrain the likelihood functional. This allows the customization of the generic burst algorithms in order to search for specific, but not very well-modeled sources. One obvious class of constraints is related to the different polarization states of the GW signals. For example, some of the core collapse models predict waveforms with a linear polarization [42] or random polarization [43]. Merging binary neutron stars or black holes are expected to produce elliptically polarized gravitational wave signals [44]. Also, the neutron star mergers can be the source of the short gamma ray burst signals [45], where relativistic jets are emitted along the rotation axis of the binary system; in this case the associated gravitational waves should have circular polarization. The cWB algorithm allows searches with
several types of polarization constraints: circular, linear, elliptical, and random (or unmodeled searches). All these searches are used in the study to estimate the possible improvement of the source localization if the reconstruction is constrained by the source model.

IV. SIMULATIONS

A. Injected signals

Several types of *ad hoc* waveforms were used to study the performance of the detector networks for different signal frequencies and polarization states. They were injected into the simulated detector data streams in a wide range of signal-to-noise ratios, with the coordinates uniformly distributed in the sky. The Gaussian detector noise was simulated with the amplitude spectral density presented in Fig. 1. The injected signals were band-limited white-noise (WNB) waveforms with random polarizations and sine-Gaussian (SG) waveforms with linear and circular polarizations. The WNB waveforms are bursts of white Gaussian noise in a frequency band (f_1, f_2) which have a Gaussian time profile with the standard deviation τ (see Table III). The random polarization waveforms h_+ and $h_\times$ were selected to have the same square-sum energy: $(h_+|h_+) = (h_\times|h_\times)$.

The SG waveforms were simulated as follows:

$$h_+(t) = h_o \sin(2\pi t f_0) \exp(-t^2/\tau^2), \tag{4.1}$$

$$h_\times(t) = h_1 \cos(2\pi t f_0) \exp(-t^2/\tau^2), \tag{4.2}$$

where f_0 is the waveform central frequency, h_o and h_1 are the waveform amplitudes, and τ is related to the waveform quality factor $Q = \sqrt{2}\pi f_0 \tau$ (see Table IV). The amplitude parameters were $h_1 = 0$ for linear polarization and $h_1 = h_o$ for circular polarization. During the analysis the amplitude

TABLE III. Simulated white-noise bursts with low frequencies (LF) and high frequencies (HF).

Waveform	τ(s)	f_1 (Hz)	f_2 (Hz)
WNB LF	0.1	250	350
WNB HF	0.1	1000	2000

TABLE IV. Simulated sine-Gaussian waveforms with quality factors $Q = 3$ and $Q = 9$, low (235 Hz or LF) and high (1053 Hz or HF) frequencies, and two polarization types—linear and circular.

Waveform	f_0 (Hz)	Q	Polarization
SGQ3 LF/HF	235/1053	3	Linear
SGQ9 LF/HF	235/1053	9	Linear
SGCQ9 LF/HF	235/1053	9	Circular

of injected events was varied to simulate events with different signal-to-noise ratios.

B. Error regions

The injected signals are used for the estimation of the accuracy of the coordinate reconstruction. For each injected event the $L_{\rm sky}$ sky map is calculated with an angular resolution of $d\Omega = 0.4 \times 0.4$ square degrees: ~200 000 sky locations (pixels) total. Figure 3 shows an example of such a sky map for one of the SGQ9 LF injections. For such events it is typical to see a pattern of fringes with a large value of $L_{\rm sky}$ corresponding to a good match between responses due to a common GW signal reconstructed in different detectors. Such sky points are the most probable source locations. Depending on many factors, such as the signal strength, waveform morphology, etc., the $L_{\rm sky}$ statistic can be well localized in a single small cluster in the sky or distributed over a large area which can also be split into several disjoint clusters. This type of ambiguity is typical for the least constrained unmodeled search and networks with only three spatially separated detectors.

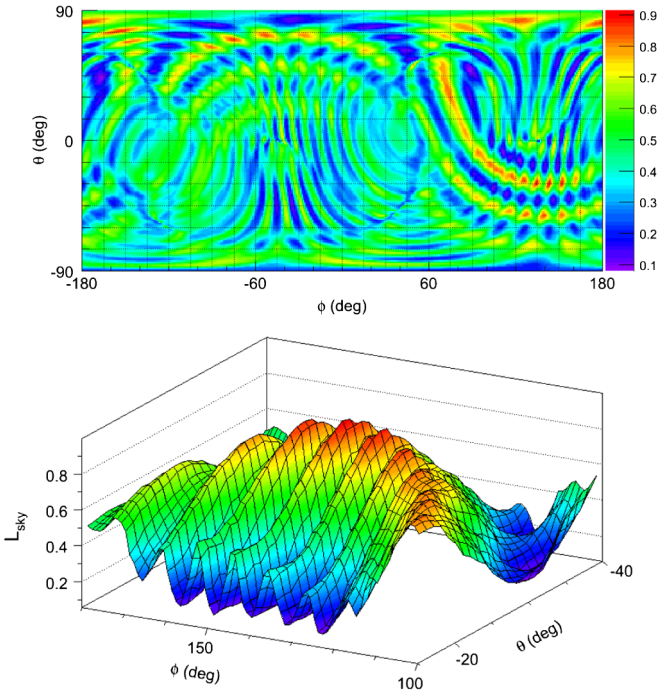

FIG. 3 (color online). Example of the likelihood sky map $L_{\rm sky}$ for an injected signal in the HLV network at $\theta = -30°$ and $\phi = 144°$: $L_{\rm sky}$ as a function of θ and ϕ (top plot), and the $L_{\rm sky}$ distribution around the reconstructed location (bottom plot).

To characterize the accuracy of the coordinate reconstruction for a single injection, we define an error region: the total area of all pixels in the sky which satisfy the condition $L_{\rm sky}(\theta, \phi) \geq L_{\rm sky}(\theta_i, \phi_i)$, where (θ_i, ϕ_i) is the injection sky location. Given a population of injected signals uniform in the sky, the 50 C.L. and 90 C.L. error regions, containing 50% and 90% of injections, respectively, can be calculated. The median error angle is defined as the square root of the 50% error area. Although the error area may be split into several disjoint areas, we often use the error angle as a convenient measure of the coordinate resolution.

The $L_{\rm sky}$ sky map can also be converted into the probability sky map which is normalized to unity if integrated over the entire sky. In this case the 50 C.L. and 90 C.L. error regions are represented by the most probable pixels with cumulative probabilities of 50% and 90%, respectively. Such probability sky maps are not relevant for the simulation studies we perform, but they are important for the analysis of real data.

V. RESULTS

A. Coordinate reconstruction

The accuracy of the coordinate reconstruction strongly depends on the strength of the detected signals which can be conveniently characterized by the average (per detector) signal-to-noise ratio

$$\rho_{\rm det} = \rho_{\rm net}/\sqrt{K}. \tag{5.1}$$

For example, Fig. 4 shows the dependence of the median error angle $\alpha_{50\%}$ on $\rho_{\rm det}$ for all injected signals, which is well approximated by a function

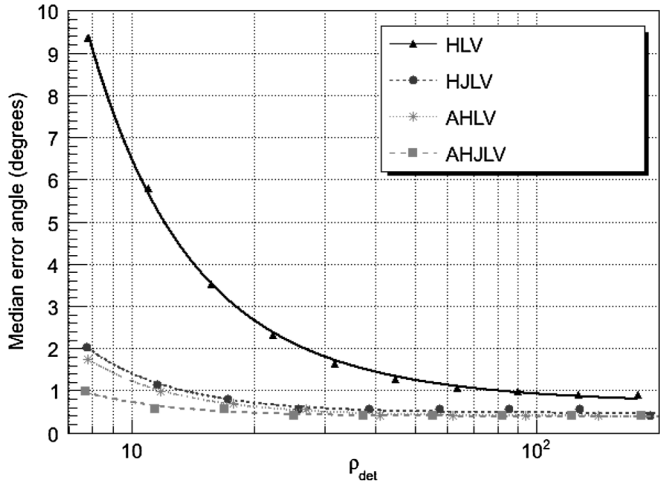

FIG. 4. Median error angle vs average detector SNR obtained with the unmodeled algorithm for all types of injections and different network configurations: HLV, AHLV, HJLV, and AHJLV.

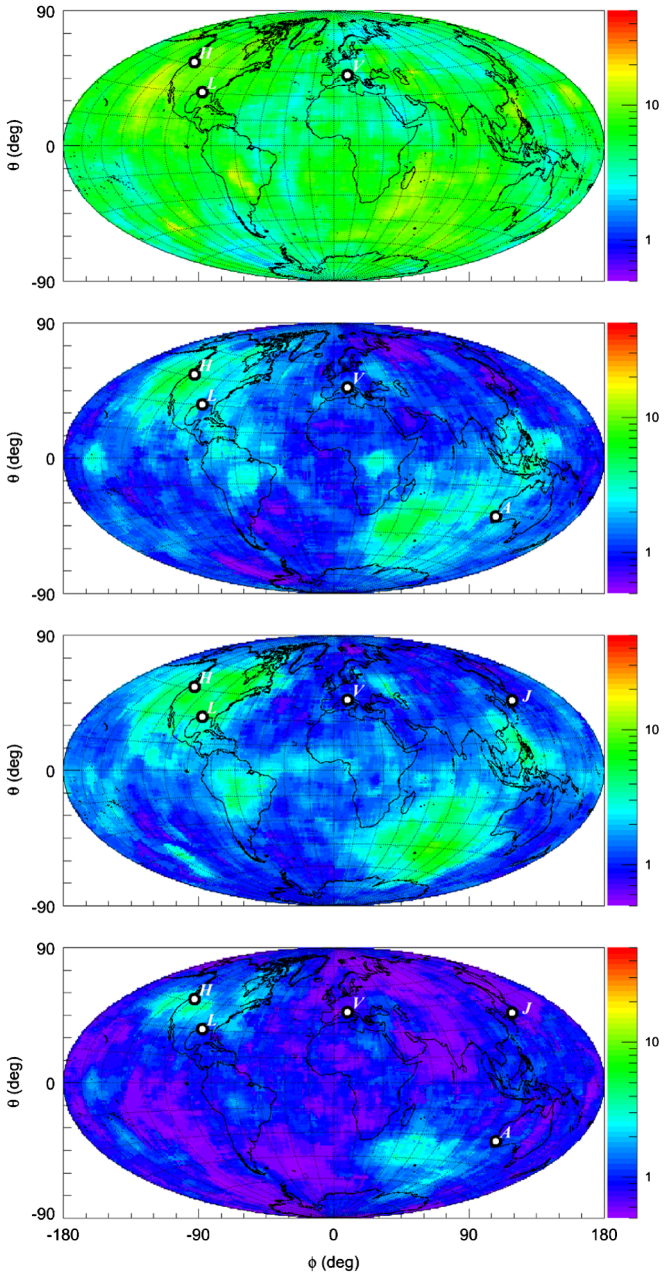

FIG. 5 (color online). Median error angle for HLV, AHLV, HJLV, and AHJLV networks (from top to bottom) as a function of source coordinates (θ—latitude, ϕ—longitude) for injections with the network SNR < 30.

$$\alpha_{50\%} = \mathrm{A} + \mathrm{B}\left(\frac{10}{\rho_{\mathrm{det}}}\right) + \mathrm{C}\left(\frac{10}{\rho_{\mathrm{det}}}\right)^2. \qquad (5.2)$$

The parameter A is the median error angle for events with very large SNR: it may not be zero due to various factors limiting the resolution (see Sec. VI). The sum of the fit parameters A + B + C is the median error angle for events with $\rho_{\mathrm{det}} = 10$. Figure 4 also shows a dependence of the coordinate resolution on the number of detector sites in the network. There is a significant improvement of the resolution when more sites are added to the network. This

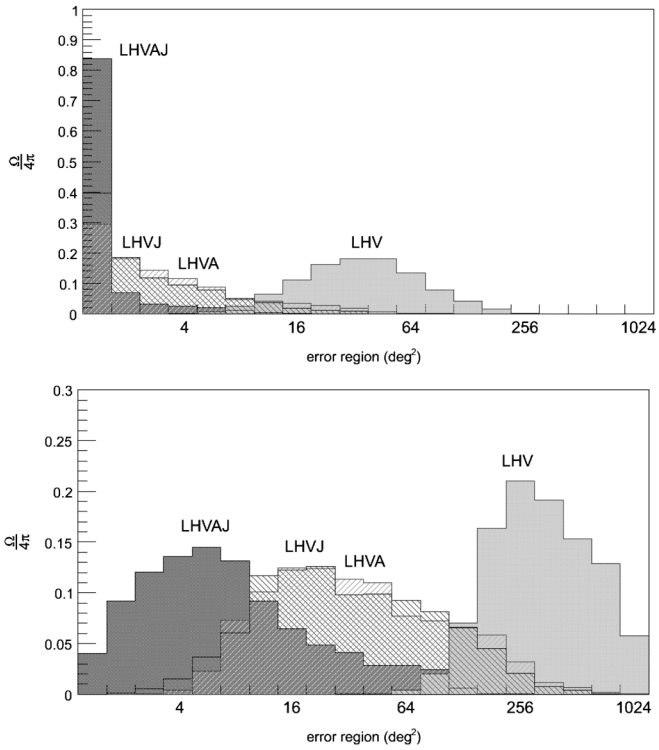

FIG. 6. Fraction of the sky (vertical axis) for three-site (LHṼV), four-site (AHLV and HJLV), and five-site (AHJLV) networks where sources (all waveform types with $\rho_{\mathrm{net}} < 30$) are reconstructed with a given 50% (top panel) and 90% (bottom panel) error region (horizontal axis).

is particularly noticeable at low SNR, which is very important because the anticipated GW signals are likely to be weak.

Because of several limiting factors (see Sec. VI) the reconstruction is not uniform in the sky. Figure 5 shows the distribution of the median error angle across the sky for different network configurations. There is a dramatic improvement of the coordinate reconstruction for the AHLV, HJLV, and AHJLV networks. However, for the four-site networks there remain areas where the source localization is poor. Figure 6 compares the pointing capabilities of the network consisting of three, four, and five sites by presenting the fraction of the sky where the reconstruction is performed with a given error area. This figure also shows a significant improvement of the source localization (particularly for the 90% error area) as more sites are used for the reconstruction. The best coordinate resolution is obtained with the five-site network, and it is compatible with the field of view of most optical telescopes.

The coordinate resolution also depends on the waveform morphology and the polarization content of GW signals (for details, see Sec. VI B). If reconstructed with the least constrained unmodeled algorithm, the SG waves with linear and circular polarization have less accurate source localization (see Fig. 7). However, the coordinate resolution can be significantly improved if the reconstruction is

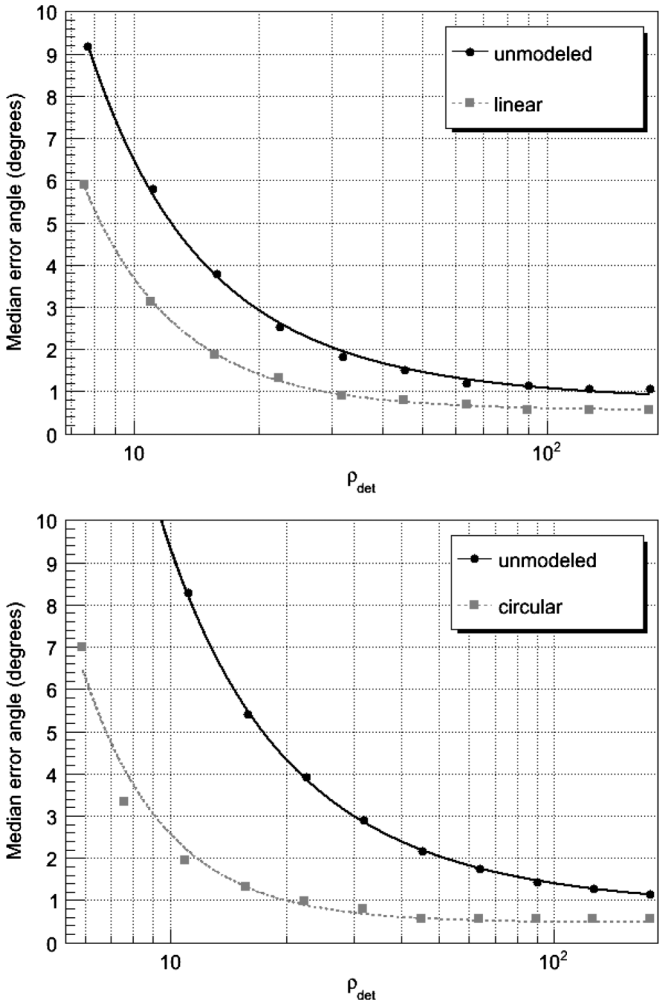

FIG. 7. Median error angle vs SNR for the HLV network comparing different constraint searches. Top panel: SGQ9 LF waveform with unmodeled (black line) and linear (grey line) searches. Bottom panel: SGCQ9 LF with unmodeled (black line) and circular (grey line) searches.

constrained by the source polarization model. In general, the reconstruction improves as more accurate models, with fewer free parameters, are used [21,31,46]. We expect, for example, that the template analysis of waves from the coalescence of binary neutron stars and black holes [47] should result in a better sky localization than for the unmodeled burst search.

Tables V, VI, VII, and VIII summarize the results of the analysis for different injection signals, source polarization models, and networks by showing the fit parameters A and A + B + C, which correspond to the median error angle for events with high and low SNRs, respectively.

B. Waveform reconstruction

The signal waveforms are obtained from the solution of the likelihood functional. They are the reconstructed detector responses as defined by Eq. (3.9). To characterize the algorithm performances on waveform reconstruction, we consider the normalized residual energy Δ:

$$\Delta = \frac{(\boldsymbol{\xi}_h - \boldsymbol{\xi}|\boldsymbol{\xi}_h - \boldsymbol{\xi})}{(\boldsymbol{\xi}_h|\boldsymbol{\xi}_h)}, \tag{5.3}$$

TABLE V. Pointing accuracy for an unmodeled search: fit parameters (A + B + C)/A represent the median error angle for events with low/high SNR.

Unmodeled	HLV	AHLV	HJLV	AHJLV
WNB LF	4.8°/0.7°	1.1°/0.4°	1.8°/0.4°	0.8°/0.4°
WNB HF	4.5°/0.4°	0.6°/0.4°	0.8°/0.4°	0.4°/0.4°
SGQ9 LF	6.4°/0.7°	1.4°/0.4°	1.6°/0.4°	1.0°/0.4°
SGQ9 HF	4.1°/0.9°	1.0°/0.4°	1.0°/0.4°	0.5°/0.4°
SGQ3 LF	9.4°/0.5°	1.1°/0.5°	1.5°/0.4°	0.9°/0.4°
SGQ3 HF	6.3°/0.4°	0.9°/0.4°	1.0°/0.4°	0.5°/0.4°
SGCQ9 LF	9.3°/0.8°	1.7°/0.4°	2.0°/0.4°	0.9°/0.4°
SGCQ9 HF	5.5°/1.1°	1.4°/0.4°	1.7°/0.4°	0.9°/0.4°

TABLE VI. Pointing accuracy for an elliptical search: fit parameters (A + B + C)/A represent the median error angle for events with low/high SNR.

Elliptical	HLV	AHLV	HJLV	AHJLV
SGQ9 LF	5.3°/0.9°	1.2°/0.4°	1.4°/0.5°	0.9°/0.4°
SGQ9 HF	4.5°/0.8°	0.8°/0.4°	0.9°/0.6°	0.5°/0.4°
SGQ3 LF	3.6°/0.6°	1.3°/0.4°	1.1°/0.4°	0.9°/0.4°
SGQ3 HF	4.4°/0.7°	0.9°/0.4°	0.8°/0.4°	0.5°/0.4°
SGCQ9 LF	8.2°/0.7°	1.9°/0.4°	1.5°/0.4°	0.9°/0.4°
SGCQ9 HF	7.2°/0.8°	1.4°/0.4°	1.1°/0.4°	0.9°/0.4°

TABLE VII. Pointing accuracy for a linear search: fit parameters (A + B + C)/A represent the median error angle for events with low/high SNR.

Linear	HLV	AHLV	HJLV	AHJLV
SGQ9 LF	3.6°/0.5°	1.1°/0.4°	1.1°/0.4°	0.7°/0.4°
SGQ9 HF	4.5°/0.6°	0.8°/0.4°	0.9°/0.4°	0.5°/0.4°
SGQ3 LF	2.7°/0.5°	1.1°/0.4°	0.9°/0.4°	0.7°/0.4°
SGQ3 HF	4.5°/0.5°	0.8°/0.4°	0.9°/0.4°	0.5°/0.4°

TABLE VIII. Pointing accuracy for a circular search: fit parameters (A + B + C)/A represent the median error angle for events with low/high SNR.

Circular	HLV	AHLV	HJLV	AHJLV
SGCQ9 LF	2.3°/0.6°	0.8°/0.4°	1.0°/0.4°	0.7°/0.4°
SGCQ9 HF	1.7°/0.6°	0.8°/0.4°	0.6°/0.4°	0.6°/0.4°

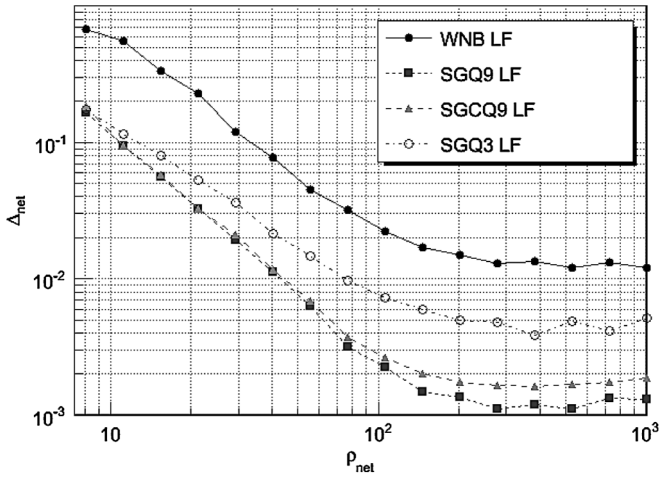

FIG. 8. Normalized residual energy Δ vs network SNR obtained with the unmodeled algorithm and the HLV network for all types of injections.

where the inner products are defined by Eq. (2.5). Like the coordinate reconstruction, the accuracy of the waveform reconstruction strongly depends on the strength of the detected signal and the waveform morphology. At low SNR, the reconstruction is affected by the detector noise; however, it improves with an increasing value of the SNR (see Fig. 8). At high SNR, the reconstruction accuracy reaches a limit due to the finite precision of the algorithm. In this paper we do not present a detailed study of the waveform reconstruction. However, such work is planned in the future.

VI. FACTORS LIMITING RECONSTRUCTION

In this section we describe the factors which limit the accuracy of the coordinate reconstruction, including (a) angular and strain sensitivity of the detectors, (b) polarization content of the signals, (c) calibration uncertainties, and (d) limitations of the reconstruction algorithm.

A. Antenna patterns and detector noise

The angular and strain sensitivity of the network is fully characterized by its noise-scaled antenna pattern vectors [see Eq. (2.1)]. Because of the unfortunate sky location or elevated detector noise, the components of these vectors corresponding to an individual detector may be small with respect to the other detectors, effectively excluding this detector from the detection and reconstruction of a marginal GW signal. For example, for a source at $(\theta = -40°, \phi = 50°)$ the angular sensitivity of the V1 detector is too low ($\sqrt{|F_+|^2 + |F_\times|^2} \sim 0$) and it cannot contribute to the reconstruction unless the GW signal is very strong. For the HLV network this means that for a significant fraction of the sky the triangulation is performed with only two detectors, which is not sufficient for the accurate source localization. For this reason it is very desirable to have four or more detectors in the network operating in coincidence.

B. Waveforms and polarization

For a given direction to the source, the reconstruction accuracy may be very different, depending on the signal polarization. For example, a linearly polarized signal $(h_+, 0)$ may not be measured by one of the detectors for some values of the polarization angle when $|F_+|$ is almost null. As a result, with the three-site networks the source localization for such signals is expected to be poor (see Fig. 9). On the contrary, signals with two polarization components can be localized well via their cross component even at the minimum of F_+.

C. Calibration uncertainties

The coordinate reconstruction may be affected by the calibration uncertainties of recorded data streams. Typically, the calibration uncertainties are of the order of 10% in the amplitude and a few degrees in the phase [48]. These systematic distortions of the GW signal may result in a systematic shift of the reconstructed sky location away from a true source location.

To estimate this effect we introduce a variation of the amplitude and phase of the injected detector responses. The amplitude variation is selected randomly between

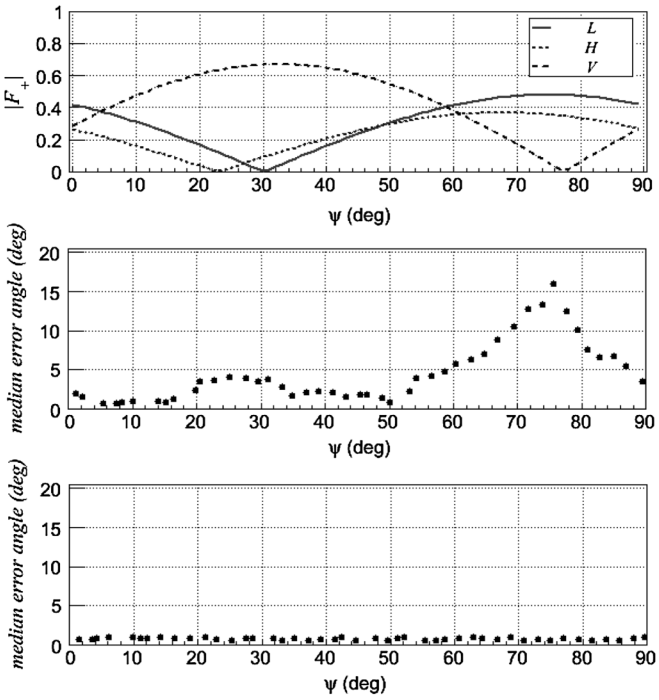

FIG. 9. Dependence of F_+ (top plot, at $\theta = -30°$ and $\phi = 72°$) and the reconstruction accuracy on the polarization angle ψ for two types of waveforms: linearly polarized SGQ9 LF waveforms (middle plot) and randomly polarized WNB LF waveforms (bottom plot).

TABLE IX. Pointing accuracy (fit parameter A) for the HLV network and different signals (column 1): no calibration errors (column 2), amplitude and phase miscalibration (columns 3 and 4, respectively).

Waveform	No error	Amplitude	Phase
WNB LF	0.7°	1.0°	0.9°
WNB HF	0.4°	0.6°	0.8°
SGQ9 LF	0.7°	2.8°	1.2°
SGQ9 HF	0.9°	1.6°	1.4°
SGQ3 LF	0.5°	2.1°	1.0°
SGQ3 HF	0.4°	1.1°	1.0°
SGCQ9 LF	0.8°	2.5°	1.1°
SGCQ9 HF	1.1°	1.9°	2.0°

$\pm 10\%$ and 0%, and the random time shifts of ± 32 μs or 0 μs are introduced. The nonzero time shifts correspond to a phase shift of $\pm 2.5°$ and $\pm 11.5°$ at the low and high frequencies, respectively. Such a ''miscalibration'' is applied to all detectors in the network. The results are reported in Table IX for the HLV network. They show that, depending on the signal morphology and bandwidth, the calibration uncertainties may affect the coordinate reconstruction. The effect of calibration uncertainties is particularly visible at high SNR where the angular resolution is less affected by the detector noise. Similar studies for the AHJLV network do not show, even at high SNR, any significant impact of the calibration errors used in the analysis. This is an expected result, because a better constrained AHJLV network provides more robust source localization than the HLV network.

D. Reconstruction algorithm

There are several factors limiting the accuracy of the coordinate and waveform reconstruction due to the cWB algorithm. For high SNR events the coordinate resolution is limited by the cWB sky segmentation, which is $0.4 \times 0.4°$. Therefore, the error angle cannot be less than $0.4°$. Also, for the high frequency events the coordinate resolution is limited by the discrete time delays τ_k (see Sec. III) with a step of $1/16\,384$ sec , and by the accuracy of the time delay filter (few percent) used in the analysis. Also, in the analysis we did not use any unmodeled constraint specific for individual networks, which, in principle, may improve the reconstruction. These limitations are not fundamental, and the algorithm performance can be improved in the future.

VII. CONCLUSION

In this paper we present the results of the source localization and reconstruction of GW waveforms with the network of GW interferometers. For a general characterization of the detector networks we introduce a few fundamental network parameters, including the effective noise, and the network antenna and alignment factors. The effective power spectral density of the network noise determines the average network SNR for a given population of GW signals. For each direction in the sky the network performance is characterized by its antenna and alignment factors. The antenna factor describes how uniform the network response across the sky is. The alignment factor, which strongly depends on the number of detectors and the orientation of their arms, determines the relative contribution of the two GW polarizations into the total network SNR.

It requires several nonaligned detectors (preferably more than three) for a robust detection and reconstruction of both GW components. The coordinate reconstruction strongly depends on the signal waveforms, network SNR, and number of detector sites in the network. The reconstruction can be significantly improved when it is constrained by the signal model. Although a crude coordinate reconstruction (ring in the sky) is possible with the networks of two spatially separated sites, at least three detector sites are required to perform the source localization. The accuracy of the localization dramatically increases for networks with more than three sites, particularly for the low SNR events. For example, the HH̃LV and AHLV networks are expected to have about the same detection rates; however, the four-site AHLV network would have much better performance for the accurate reconstruction of GW signals. The pointing resolution required for joint observations with the electromagnetic telescopes is achievable with the networks consisting of four sites. The AHJLV network demonstrates further improvements, both in the detection and reconstruction of GW signals, reaching a subdegree angular resolution. In addition, due to the limited duty cycle of the detectors, both the LCGT and the Australian detectors will significantly increase the observation time when any of the four-site networks are operational.

The advanced LIGO and Virgo detectors are very capable of the first direct detection of gravitational waves. However, for better reconstruction of the GW signals more detectors are required. Extra detectors introduce an important redundancy which lowers the impact of the limited duty cycle of the detectors, and makes the coordinate reconstruction more accurate and less dependent on the waveform morphology and calibration uncertainties. The construction of the LCGT and the detector in Australia will significantly enhance the advanced LIGO-Virgo network, and these detectors will play a vital role in the future GW astronomy.

ACKNOWLEDGMENTS

The authors are thankful to the LIGO-Australia committee members R. Weiss, P. Saulson, S. Sathyaprakash, F. Raab, P. Fritschel, and S. Finn for useful discussions of the results. Also, the authors appreciate suggestions by L. Bildsten for a better presentation of the results, particularly in Fig. 6. This work was supported by the U.S. National Science Foundation Grants No. PHY-0855044 and No. PHY-0855313 to the University of Florida, Gainesville, Florida.

[1] B. P. Abbott *et al.*, Rep. Prog. Phys. **72**, 076901 (2009).
[2] F. Acernese *et al.*, Classical Quantum Gravity **23**, S635 (2006).
[3] J. Abadie *et al.*, arXiv:1003.2481v3.
[4] B. P. Abbott *et al.*, Phys. Rev. D **80**, 047101 (2009).
[5] J. Kanner *et al.*, Classical Quantum Gravity **25**, 184034 (2008).
[6] R. Fender *et al.*, Proc. Sci. **MQW6**, 104 (2006).
[7] http://www.naic.edu.
[8] N. Gehrels, J. K. Cannizzo, and J. P. Norris, New J. Phys. **9**, 37 (2007).
[9] C. W. Akerlof *et al.*, Publ. Astron. Soc. Pac. **115**, 132 (2003).
[10] C. Baltay *et al.*, Publ. Astron. Soc. Pac. **119**, 1278 (2007).
[11] A. Klotz, M. Bor, J. L. Atteia, and B. Gendre, Astron. J. **137**, 4100 (2009).
[12] M. Ageron *et al.* (ANTARES Collaboration), Astropart. Phys. **31**, 277 (2009).
[13] R. Abbasi *et al.* (IceCube Collaboration), Astrophys. J. **701**, L47 (2009).
[14] J. Abadie *et al.*, Classical Quantum Gravity **27**, 173001 (2010).
[15] http://www.lsst.org/lsst.
[16] N. Kaiser *et al.*, Proc. SPIE Int. Soc. Opt. Eng. **4836**, 154 (2002).
[17] http://www.tmt.org/.
[18] P. Jaranowski and A. Krolak, Phys. Rev. D **49**, 1723 (1994).
[19] J. Markowitz, M. Zanolin, L. Cadonati, and E. Katsavounidis, Phys. Rev. D **78**, 122003 (2008).
[20] S. Fairhurst, New J. Phys. **11**, 123006 (2009).
[21] L. Wen and Y. Chen, Phys. Rev. D **81**, 082001 (2010).
[22] Y. Gürsel and M. Tinto, Phys. Rev. D **40**, 3884 (1989).
[23] É. E. Flanagan and S. A. Hughes, Phys. Rev. D **57**, 4566 (1998).
[24] S. Klimenko, S. Mohanty, M. Rakhmanov, and G. Mitselmakher, Phys. Rev. D **72**, 122002 (2005).
[25] S. Klimenko *et al.*, Classical Quantum Gravity **25**, 114029 (2008).
[26] A. C. Searle, P. J. Sutton, and M. Tinto, Classical Quantum Gravity **26**, 155017 (2009).
[27] D. Buskulic (LIGO and Virgo Collaborations), Classical Quantum Gravity **27**, 194013 (2010).
[28] B. F. Schutz and M. Tinto, Mon. Not. R. Astron. Soc. **224**, 131 (1987).
[29] A. C. Searle, S. M. Scott, D. E. McClelland, and L. S. Finn, Phys. Rev. D **73**, 124014 (2006).
[30] R. Weiss *et al.* (LIGO Scientific Collaboration), LIGO Document No. T1000251-v1, https://dcc.ligo.org/cgi-bin/DocDB/ShowDocument?docid=11604.
[31] B. F. Schutz, arXiv:1102.5421.
[32] M. Ando *et al.*, Phys. Rev. D **71**, 082002 (2005).
[33] H. Luck *et al.*, Classical Quantum Gravity **23**, S71 (2006).
[34] G. M. Harry, and the LIGO Scientific Collaboration, Classical Quantum Gravity **27**, 084006 (2010).
[35] F. Acernese *et al.* (Virgo Collaboration), Report No. VIR0027A09, https://pub3.ego-gw.it/itf/tds/file.php?callFile=VIR-0027A-09.pdf.
[36] T. Uchiyama (LCGT Collaboration), Classical Quantum Gravity **21**, S1161 (2004).
[37] K. Kuroda (LCGT Collaboration), Classical Quantum Gravity **27**, 084004 (2010).
[38] D. G. Blair (AIGO Collaboration), J. Phys. Conf. Ser. **122**, 012001 (2008).
[39] L. A. Wainstein and V. D. Zubakov, *Extraction of Signals from Noise* (Dover, New York, 1970).
[40] If $x_k[i]$ are produced with a windowed Fourier transformation, the sum is taken over the positive and negative frequencies.
[41] J. Abadie *et al.*, Phys. Rev. D **81**, 102001 (2010).
[42] C. Ott, A. Burrows, L. Dessart, and E. Livne, Phys. Rev. Lett. **96**, 201102 (2006).
[43] C. Ott, Classical Quantum Gravity **26**, 063001 (2009).
[44] C. Pankow *et al.*, Classical Quantum Gravity **26**, 204004 (2009).
[45] B. P. Abbott *et al.*, Astrophys. J. **681**, 1419 (2008).
[46] S. Fairhurst, arXiv:1010.6192.
[47] B. P. Abbott *et al.*, Phys. Rev. D **82**, 102001 (2010).
[48] J. Abadie *et al.*, Nucl. Instrum. Methods Phys. Res., Sect. A **624**, 223 (2010).